

## Nanothermal characterization of amorphous and crystalline phases in chalcogenide thin films with scanning thermal microscopy

J. L. Bosse, M. Timofeeva, P. D. Tovee, B. J. Robinson, B. D. Huey, and O. V. Kolosov

Citation: [Journal of Applied Physics](#) **116**, 134904 (2014); doi: 10.1063/1.4895493

View online: <http://dx.doi.org/10.1063/1.4895493>

View Table of Contents: <http://scitation.aip.org/content/aip/journal/jap/116/13?ver=pdfcov>

Published by the [AIP Publishing](#)

---

### Articles you may be interested in

[Three dimensional finite element modeling and characterization of intermediate states in single active layer phase change memory devices](#)

[J. Appl. Phys.](#) **117**, 214302 (2015); 10.1063/1.4921827

[The effect of Ta interface on the crystallization of amorphous phase change material thin films](#)

[Appl. Phys. Lett.](#) **104**, 221605 (2014); 10.1063/1.4881927

[Inducing chalcogenide phase change with ultra-narrow carbon nanotube heaters](#)

[Appl. Phys. Lett.](#) **95**, 243103 (2009); 10.1063/1.3273370

[Crystal morphology and nucleation in thin films of amorphous Te alloys used for phase change recording](#)

[J. Appl. Phys.](#) **98**, 054902 (2005); 10.1063/1.2034655

[Electrical percolation characteristics of Ge<sub>2</sub>Sb<sub>2</sub>Te<sub>5</sub> and Sn doped Ge<sub>2</sub>Sb<sub>2</sub>Te<sub>5</sub> thin films during the amorphous to crystalline phase transition](#)

[J. Appl. Phys.](#) **97**, 083538 (2005); 10.1063/1.1875742

---

Did your publisher get  
**18 MILLION DOWNLOADS** in 2014?  
AIP Publishing did.



THERE'S POWER IN NUMBERS. Reach the world with AIP Publishing.



# Nanothermal characterization of amorphous and crystalline phases in chalcogenide thin films with scanning thermal microscopy

J. L. Bosse,<sup>1</sup> M. Timofeeva,<sup>2</sup> P. D. Tovee,<sup>3</sup> B. J. Robinson,<sup>3</sup> B. D. Huey,<sup>1</sup>  
 and O. V. Kolosov<sup>3,a)</sup>

<sup>1</sup>*Department of Materials Science & Engineering, University of Connecticut, Storrs, Connecticut 06269-3136, USA*

<sup>2</sup>*Nanotechnology Centre, St. Petersburg Academic University, Chlopina 8/3, 194021 St. Petersburg, Russia*

<sup>3</sup>*Department of Physics, Lancaster University, Lancaster LA1 4YB, United Kingdom*

(Received 18 June 2014; accepted 31 August 2014; published online 2 October 2014)

The thermal properties of amorphous and crystalline phases in chalcogenide phase change materials (PCM) play a key role in device performance for non-volatile random-access memory. Here, we report the nanothermal morphology of amorphous and crystalline phases in laser pulsed GeTe and Ge<sub>2</sub>Sb<sub>2</sub>Te<sub>5</sub> thin films by scanning thermal microscopy (SThM). By SThM measurements and quantitative finite element analysis simulations of two film thicknesses, the PCM thermal conductivities and thermal boundary conductances between the PCM and SThM probe are independently estimated for the amorphous and crystalline phase of each stoichiometry. © 2014 AIP Publishing LLC. [<http://dx.doi.org/10.1063/1.4895493>]

## INTRODUCTION

Phase change materials (PCM) have been the focus of research interest for the last decade as candidates for non-volatile memories, such as flash memory and dynamic random access memory, as they can combine high read/write speeds, excellent data retention, and low switching power.<sup>1</sup> Phase change memory is based on reversible switching between amorphous and crystalline states,<sup>2</sup> producing remarkable reflectivity contrast for optical devices,<sup>3,4</sup> and electrical conductivity modulation for solid state devices.<sup>5,6</sup> Finding stoichiometries that promote a fast crystallization time, lower threshold switching voltage/current between states, and improved high-cycle reliability are of particular interest.<sup>7</sup> Although various scanning probe microscopy (SPM) techniques have been employed to study these materials by electrical<sup>1,8–11</sup> and nanomechanical<sup>12,13</sup> means, these do not include a quantitative, non-destructive characterization method to investigate the local nanoscale thermal properties of PCM—a critical factor defining their switching energy and read/write dynamics. Several methods are currently employed to study thermal properties, such as Raman spectroscopy and IR spectroscopy, however, these have a spatial resolution limited to the micrometre scale.<sup>14,15</sup> Scanning Thermal Microscopy (SThM),<sup>16</sup> on the other hand, would provide an ideal platform for quantitative measurement and mapping of local thermal properties of phase change materials and devices, with the added potential capability of directly reading and writing “bits” of data (phase changed regions) with spatial resolution down to the nanometer scale.<sup>17,18</sup>

In the present work, we demonstrate a SThM approach for the study of the thermal properties of amorphous (a) and crystalline (c) phases of commercially viable PCM stoichiometries, Ge<sub>2</sub>Sb<sub>2</sub>Te<sub>5</sub> (a-GST/c-GST) and GeTe (a-GT/c-GT). These are selected as they demonstrate nucleation and

growth dominated crystallization behavior, respectively.<sup>19</sup> The thermal responses for the amorphous and crystalline phases are modeled and the thermal conductivities compared with a range of previously reported values. This work is of particular interest to research efforts on determining the phase switching thresholds for phase change materials as a function of varying experimental parameters, such as composition gradients, sample thickness, applied voltage, or power.

## MATERIALS AND METHODS

### Sample fabrication and laser writing of crystalline domains

Films of 100 and 200 nm thickness were RF-sputtered (Moorfield MiniLab 25) on soda-lime glass coverslips substrate held at room temperature. The substrates were covered with a 10 nm Ti bonding layer that was an order of magnitude thinner than the PCM film in order to minimize its influence on the measured thermal properties; such deposition is reported<sup>20,21</sup> to produce practically fully amorphous GT and GST films. Samples were subsequently mounted onto a motorized XYZ stage and illuminated with a focused 514 nm wavelength Ar ion laser of varying power from 3 to 4 mW on the sample (Spectra Physics). The laser power was on-off modulated with a mechanical chopper to produce pulses of 200 μs and longer duration, and programmatically translated with a step motor controller (Honda Electronics) at 50 μm per second. Such arrangement was shown to produce crystalline lines in the amorphous films across all layer thicknesses with a consistent heating per unit area as described elsewhere.<sup>12,13</sup>

### SThM calibration, thermal imaging, and tip-sample thermal conductance measurements

SThM images were acquired on the amorphous and crystalline phases of both film thicknesses, allowing the investigation of the nanoscale thermal properties and their

<sup>a)</sup>Electronic mail: o.kolosov@lancaster.ac.uk

morphology. All SThM measurements were acquired in ambient environment using a commercial SPM (Bruker MultiMode Nanoscope III controller) and dedicated SThM probe holder (Anasys Instruments). Thermal transport measurements were performed using resistive SThM probes (Kelvin Nanotechnology, KNT-SThM-01a, 0.3 N/m spring constant, <100 nm tip radius) in the Wheatstone bridge configuration, with applied DC offset generating Joule heat in the probe,<sup>22,23</sup> and resistance measured using AC resistance measurements via lock-in amplifier (SRS Instruments) at 90 KHz frequency therefore optimizing signal-to-noise ratio.<sup>24</sup> The probe was thermally calibrated on a Peltier hot/cold plate (Torrey Pines Scientific, Echo Therm IC20), linking probe resistance and probe temperature using a ratiometric approach (Agilent 34401A) described in details elsewhere<sup>24</sup> that allowed us to independently quantify the heat generated by the probe and probe temperature. The standard SPM laser illumination necessary for measuring probe deflection was heating the probe by additional 10 °C, effectively adding to the Joule heating of the probe and was accounted in the measurements. SThM thermal mapping was performed with a set-force below 15 nN during imaging to protect the tip and sample from damage to either structure.

During qualitative thermal mapping, the SThM probe is scanned across the sample surface, in continuous contact, while the power of the probe is kept constant. The changes in the probe temperature are presented in SThM image as darker (brighter) areas corresponding to increased (decreased) sample thermal conductivity.

For quantitative measurements, the probe is located above a particular point of the sample surface and repeatedly slowly brought into and out of contact with the surface, producing so called “approach-retract curves”<sup>25</sup> with the force acting on the probe and the probe temperature monitored simultaneously. By comparing the heat flow from the probe immediately before and after the contact, it is possible to quantitatively determine the thermal resistance (or its inverse, thermal conductance) of the probe-sample contact<sup>16,24,26</sup> and to subsequently determine the thermal conductivity of the probed material.

For quantification of thermal properties, the equivalent thermal resistance between the probe and its surroundings,

$R_T$ , is considered according to previous models (Fig. S2<sup>27</sup>) as defined by the following equation:<sup>16,24</sup>

$$R_T = \frac{T_H - T_0}{Q_h}, \quad (1)$$

where  $T_H$  and  $T_0$  is the heater and ambient temperature, respectively, and  $Q_h$  is the heat generated by the heating element. It has been shown previously<sup>28,29</sup> that one of the most important factors is the tip/sample thermal boundary conductance  $\sigma_{ts}$  (TBC), that is the inverse of the thermal boundary resistance  $R_{ts} = \sigma_{ts}^{-1}$  also known as “Kapitza resistance.”<sup>30–33</sup> The SThM response is strongly dependent on both  $R_{ts}$  as well as the sample thermal conductivity; by selecting a PCM film of 100 to 200 nm thickness and a substrate with low thermal conductivity (soda lime glass), the heat transport in the film was found to dominate the SThM response, demonstrating clear SThM sensitivity to the varying properties of the PCM. Additionally, by performing SThM measurements on two different film thicknesses and assuming a thickness independent TBC (a reasonable approximation as the mean free path (MFP) of the heat carriers in PCM is much shorter than the film thicknesses studied),<sup>34,35</sup> the true sample thermal conductivity may be extracted from the experimental SThM data.

### Multi-scale finite element modeling of probe-sample thermal interactions

A detailed three dimensional finite element analysis (FEA) was performed using commercial software (COMSOL Multiphysics, Joule Heating and MEMS modules). This allowed us to determine the influence of the cantilever/sample geometry and sample materials properties on the SThM experimental results and to evaluate the thermal conductivities of the amorphous and crystalline phases. The FEA model is based on the experimental setup as described, with a SThM cantilever, GST or GeTe thin film, soda-lime-silica glass substrate, and Ti interlayer between the PCM and substrate. The proportions and materials used for the modeled SThM cantilever were similar to those implemented in the experiments, Fig. 1(a), with 250 nm Au pads and 150 nm Pd resistors micro-patterned on a commercial  $\text{Si}_3\text{N}_4$

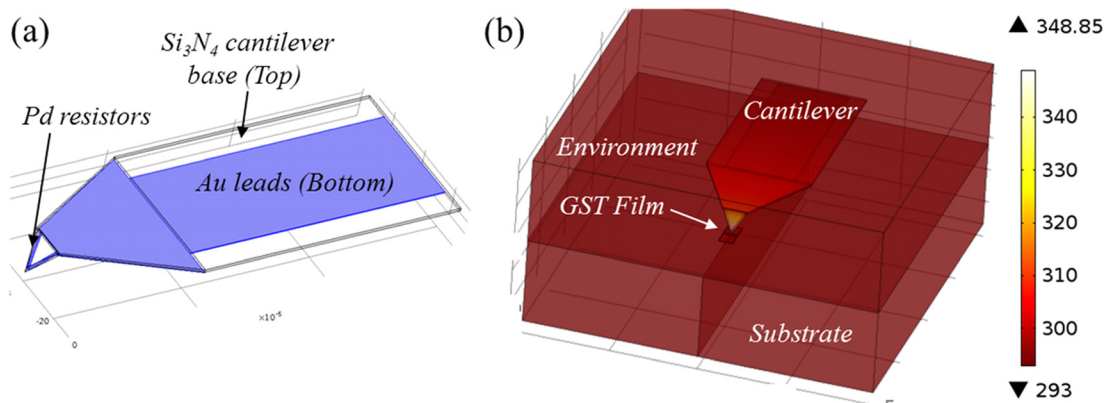


FIG. 1. (a) The design of the SThM probe with  $\text{Si}_3\text{N}_4$  cantilever base, Au pads, and Pd resistors reflected in the simulation. (b) The model system comprising a cantilever approaching a PCM film on a soda lime glass substrate, and the ambient air environment.

cantilever base.<sup>24</sup> The modeled PCM samples consist of a  $2\ \mu\text{m} \times 8\ \mu\text{m}$  crystalline phase positioned between two  $8\ \mu\text{m} \times 8\ \mu\text{m}$  amorphous phases, with a layer thickness equal to either 100 or 200 nm. The cantilever and sample were placed in an air block, and the temperature profile of the entire three-dimensional system was calculated, Fig. 1(b), as described elsewhere.<sup>24</sup> The thermal conductivities for all materials used in the 3D model are presented in Table I. Note that the thermal conductivities of the sputtered Au pads and  $\text{Si}_3\text{N}_4$  cantilever base, with effective values of 170 and  $4.5\ \text{Wm}^{-1}\text{K}^{-1}$ , respectively, are determined by matching the heat-temperature balance and conductance values of the SThM probe in air (within 0.25–0.50 K at 293 and 353 K) with experimental data as described elsewhere<sup>24</sup> for both hot plate and self-heating calibration measurements, while accounting for the electrical circuit of the probe containing two 100  $\Omega$  resistors in series with the heater.

It should be noted that the characteristic dimensions of the modeled system used in our study were 100 nm (for thinner film) or above. This was significantly larger than the phonon MFP for both amorphous (5 Å) and crystalline (20 Å) GeTe.<sup>35–37</sup> For crystalline material, such as GeTe, some fraction of thermal conductivity is known to be electron related<sup>38</sup> with a corresponding MFP estimated to be below 50 nm.<sup>35</sup> Therefore, we consider the diffusive heat flow approximation used in this study to be appropriate for modelling of such systems.

The tip-sample TBC may be presented as

$$\sigma_{ts} = \rho_c \pi r_{ts}^2, \quad (2)$$

where  $\rho_c$  and  $r_{ts}$  are the conductance and effective interface radius of the contact between the tip and sample, respectively. To incorporate the TBC in the FEA simulation, we include a thin resistive layer between the tip apex and the sample represented by a cylinder with height ( $h$ ) much smaller than the contact diameter ( $2r_{ts}$ ). The thermal conductivity of the TBC is then calculated as

$$\sigma_{ts} = h\rho_c. \quad (3)$$

All heat transfer processes in his study were performed on the time scale from 200  $\mu\text{s}$  (laser induced heating) to sub-seconds (SPM approach-retract cycles). Both of these are several orders of magnitude longer than the characteristic time for the heat transfer in both 100 and 200 nm thick amorphous and crystalline GeTe films, estimated to be below 100 ns.<sup>12</sup> Therefore, we can safely use the time-independent standard stationary diffusive approximation heat transport equation<sup>39</sup>

TABLE I. Thermal conductivities ( $\text{Wm}^{-1}\text{K}^{-1}$ ) for materials used in the FEA model.

Pd	Soda-lime glass	Air	Ti	Au	$\text{Si}_3\text{N}_4$
71 (Ref. 40)	1.05 (Ref. 41)	0.02 (Ref. 42)	21.9 (Ref. 40)	170 <sup>a</sup>	4.5 <sup>a</sup>

<sup>a</sup>Note that effective values are used for Au and  $\text{Si}_3\text{N}_4$  thin films to match the experimentally measured probe thermal and electrical resistances for the hot plate and self-heating calibration measurements.

$$\rho C_p \frac{\partial T}{\partial t} = k\nabla T + \mathbf{q}, \quad (4)$$

where  $\rho$  is the density of the material,  $C_p$  is the heat capacity at constant pressure,  $k$  is the media thermal conductivity, and  $\mathbf{q}$  is the heat flux. As the temperature distribution is assumed to be time independent due to the slow ramp rate of the force-distance curves, the left-hand side of Eq. (4) equates to zero. By solving Eq. (4) for all structural parts of the system<sup>27</sup> and with the proper boundary conditions, we then obtain the modeled temperature distribution. The thermal boundary conditions were set such that the temperature of the surrounding environment as well as the initial temperature of all domains was 293 K. A fixed electrical potential difference is applied across Pd resistors at the probe apex as identified in Fig. 1(a) (the only domain in the model to include an electrical component) to induce local Joule heating reflecting experimental conditions. Finally, the thermal discontinuity experienced by the probe when brought into contact or out of contact was calculated and compared with that of corresponding experimental data. By adjusting the thermal properties of the modeled amorphous and crystalline phases to match the SThM experimental results, the measured amorphous and crystalline PCM thermal properties are estimated.

## RESULTS AND DISCUSSIONS

### Two-dimensional SThM mapping of PCM thermal conductance

Fig. 2(a) presents experimentally obtained topography (left) and corresponding SThM (right) images for the 200 nm GT specimen with 10 and  $2.5\ \mu\text{m}$  scan sizes, respectively. Figs. 2(b) and 2(d) presents similar results for the 200 nm GST specimen, but with 8 and  $2.5\ \mu\text{m}$  scan sizes, respectively. The SThM images display the temperature of the SThM sensor, henceforth labeled as “thermal images” with constant power applied to the probe. The darker contrast in Fig. 2 corresponds to the low SThM signal and hence low probe temperature meaning low thermal contact resistance due to high sample thermal conductivity. Topographically, the depressions running down the centers of the height images correspond to the crystalline phases nucleated in the surrounding amorphous film by the laser as it traversed the film. Such a specific volume reduction between amorphous and crystalline phases is expected, and is typically 5% for these stoichiometries<sup>43</sup> and in line with the expected full crystallization of these PCM at line recording parameters (see Materials and Methods).

For the SThM images, the thermal response is uniformly darker for the crystalline phase compared with the surrounding amorphous film, indicating a change of the total tip-sample thermal resistance that is the combination of the thermal boundary resistance and the sample spreading thermal resistance,  $R_{ts} + R_s$ , and which is clearly lower in crystalline compared with the amorphous regions.

There are two noteworthy aspects related to the morphology at the boundary between the amorphous and crystalline phases. The higher magnification SThM images in

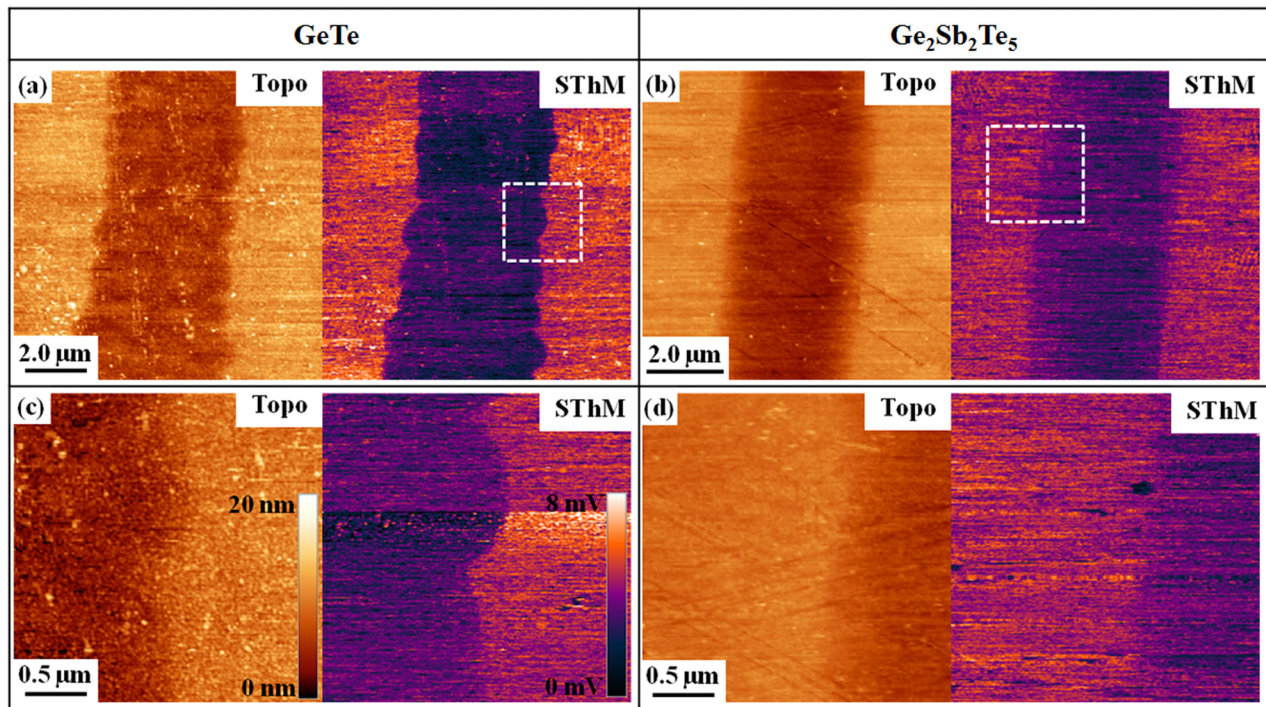


FIG. 2. (a) Topography (left sub-panel) and SThM (right sub-panel) images with  $10\ \mu\text{m}$  and (b)  $8\ \mu\text{m}$  scan sizes, revealing a crystalline line written into 200 nm GT and GST amorphous thin films by a focused laser beam. (c) The  $2.5\ \mu\text{m}$  images for GT and (d) GST taken from the spatial locations marked by the insets in (a) and (b).

Figs. 2(c) and 2(d) indicate that the boundary is sharper for GT than GST. Fig. 2(c) reveals a 30 to 50 nm transition between the crystalline and amorphous regions for GT. For GST, on the other hand, the tip-sample thermal resistance change over the boundary from crystalline to amorphous regions occurs over 80 to 440 nm, Fig. 2(d). Furthermore, the crystal/amorphous boundary represents a relatively straight line for the GST film, while for GT, it has clear deviations from such line. While some line undulation may be expected due to the discrete motion of the step motor, the fact that it is more prominent for the GT film may relate to the growth dominated crystallization behavior for GT as compared with GST, causing more variability in GT phase boundaries once nucleation sites have become activated.

### Quantitative analysis of PCM thermal properties

To quantify the values of total tip-sample thermal resistance, we used “force-vs-distance” and “probe temperature-vs-distance” curves acquired when the SThM tip repeatedly approaches the surface, touches the surface establishing direct thermal contact and then retracts (see Materials and Methods). During such cycles, we record the SPM stage displacement that modifies the distance between the SThM probe and the sample, the cantilever deflection that is proportional to the normal force acting on the tip and indicate the moment that tip-surface contact is established, and the thermal signal throughout the cycle. Figs. 3(a) and 3(b) present such force-distance curves for 200 nm crystalline and amorphous GST films, respectively, with the tip approaching from the left, snapping in to contact leading to a slight decrease in deflection, then linearly deflecting positively as

the displacement increases further, indicating that the SThM lever is highly compliant compared with the sample. Figs. 3(c) and 3(d) present the simultaneously acquired thermal signals, during approach (dashed) and retraction (solid) directions. While approaching the sample, the thermal signal decreases linearly until the point of tip/sample contact (compared with the snap-in displacements from Figs. 3(a) and 3(b)), at which point the signal abruptly decreases due to the added tip-sample thermal conductance. During tip retraction, adhesion forces maintain contact until pull-off occurs as is typical for AFM-based measurements in ambient conditions. The thermal signal again changes sharply, now due to loss of contact, after which the thermal response matches the previous, non-contact values.

When comparing the crystalline (Fig. 3(c)) with amorphous (Fig. 3(d)) thermal approach curves, the thermal drop is notably stronger for the crystalline phase, consistent with the SThM imaging performed in Fig. 2 where the crystalline regions exhibit lower signals. To quantify this parameter more thoroughly, such sharp drops and the subsequent rise in the thermal response for approach and retract, respectively, were averaged for several groups of successive force-distance curves ( $N = 3$ ) and analyzed for each stoichiometry, specimen thickness, and amorphous/crystalline phase. The approach portion of these experimental results was then compared with thermal modeling for equivalent conditions. It is worth noting that the retract curves could have also been used for comparison with the thermal modeling, as experimentally they display similar trends as observed in Fig. 3. However, the magnitudes of the thermal jumps are generally less reliable since retraction curves also depend on adhesion effects during tip/sample pull-off. An increase in adhesion

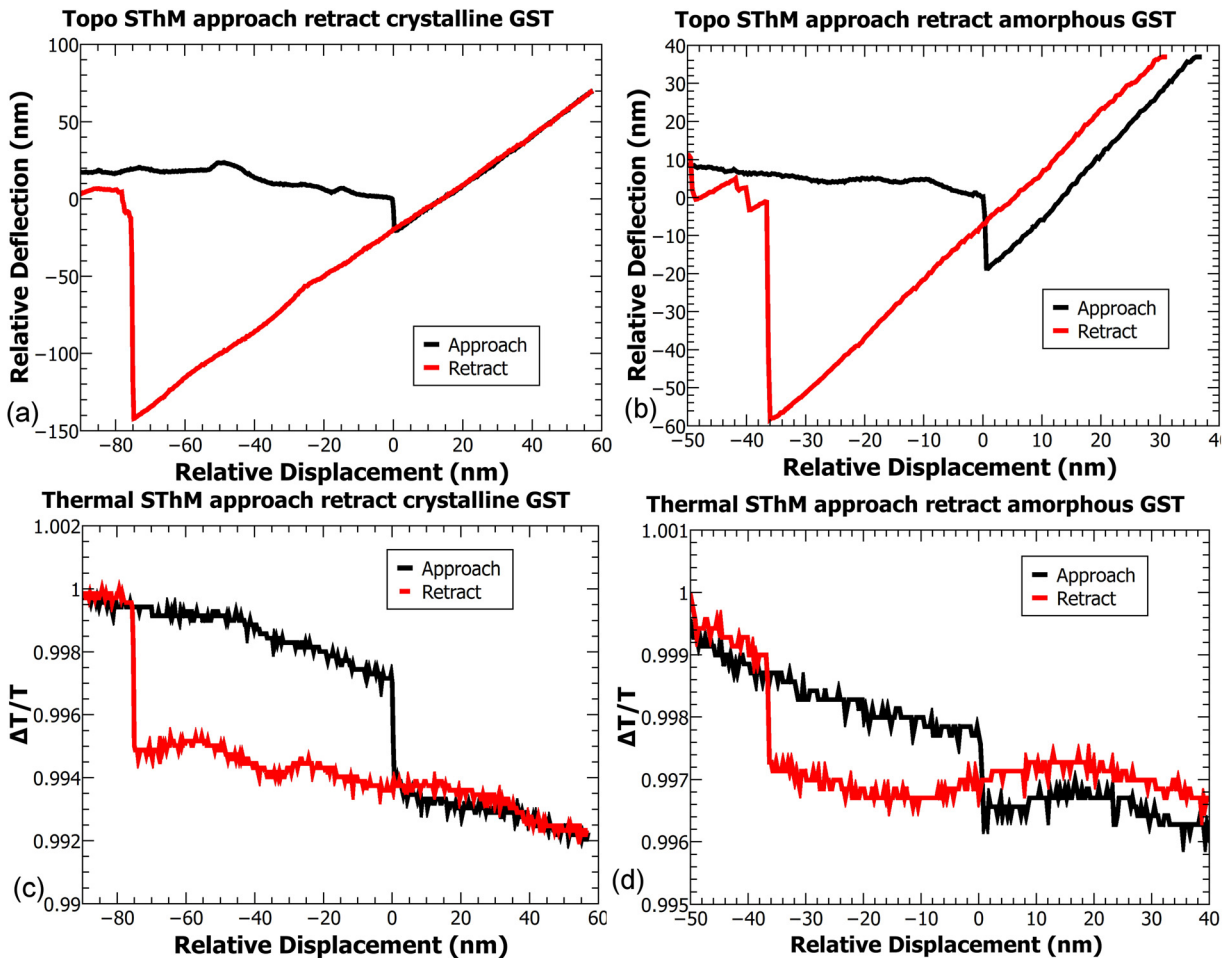


FIG. 3. The typical approach and retract SThM curves for PCM materials, with simultaneously recorded relative cantilever deflection (a) and (b) and thermal (c) and (d) signal as a function of relative displacement for contact with crystalline (a) and (c) and amorphous (b) and (d) GST phases.

would thus produce a larger pull-off displacement ( $\sim 75$  vs.  $\sim 40$  nm for crystalline and amorphous GST, respectively, in Fig. 3), and hence a greater pull-off deflection ( $\sim 150$  vs.  $\sim 60$  nm), distorting interpretation of the corresponding thermal jump as if a higher thermal conductivity was encountered. The snap-to-contact displacement, and deflection, for approach curves are susceptible to adhesion to a much smaller degree with nearly uniform change in lever deflection ( $\sim 20$  nm). Therefore, any error caused by such adhesion-based artifacts (if present) is minimized for approach curves that are therefore preferred for the SThM quantitative measurements.

The observed thermal “drops” upon contact with the crystalline phases are consistently larger regardless of film thickness than ones for amorphous phases, for both GST and GT (not shown for brevity). However, the contrast between the crystalline and amorphous phase is stronger for thicker PCM films, as anticipated due to the larger contribution of the film with respect to the underlying glass substrate. Since tip-sample TBC  $R_{ts}$  should be identical for both measurements, as noted above, whereas the thermal resistance of the film  $R_s$  differs with the film thickness, the tip-sample contact resistance as well as TBC can be independently extracted with appropriate models owing to the measurements of two different thicknesses of the same material. The obtained

TBC can also be compared with one determined via the acoustic mismatch model (AMM).<sup>31</sup> Finally, the modeled thermal “drops” on tip-surface contact are fitted to match the experimental values.

### FEA simulations of SThM response to PCM thermal conductivity

The temperature distribution of the modeled SThM system is presented for the SThM probe out of contact (Fig. 4(a)) and in contact (Fig. 4(b)) with c-GST, as well as out of contact (Fig. 4(c)) and in contact (Fig. 4(d)) with a-GST. The model accounts for the substrate, underlying adhesion layer, PCM film, environment, probe geometry near the apex, and distinct probe materials, including a silicon nitride tip and cantilever, gold current leads as well as the resistive heating elements.

For contact with the crystalline GST film, heat is conducted easily from the probe in the plane of the film and through the glass substrate. This predicts the largest temperature drop of the probe, as measured experimentally. For contact with the amorphous GST film, on the other hand, the higher thermal resistance limits heat dissipation in-plane as well as into the glass substrate, retaining more heat locally. As a result, a weaker thermal drop is predicted, and

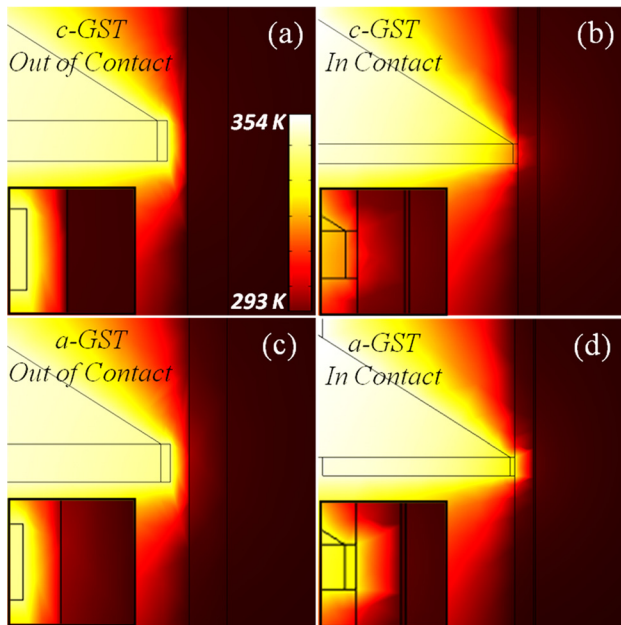


FIG. 4. Cross-section view of the simulated temperature distribution between the SThM probe and sample. (a) Out-of-contact and (b) in-contact data for 100 nm c-GST vs out-of-contact (c) and in-contact (d) of 100 nm a-GST film. The out of contact tip-sample distance is 50 nm, the temperature scale bar applies to all cases. Although not fully visible in (a) and (c), the 10 nm Ti layer is present and incorporated into the temperature distribution model.

experimentally measured. When out of contact, the highest temperature of the probe is observed, with minimal heat loss to the PCM and underlying glass substrate, as expected. Nevertheless, for near-contact conditions as modeled (50 nm separation), the a-GST (Fig. 4(c)) is noticeably hotter than the c-GST out of contact (Fig. 4(a)). c-GT and a-GT temperature distributions follow a similar trend.

### Evaluation of PCM layer thermal conductance via comparison of experimental data and FEA analysis

The relative thermal drops (ratio of change of the probe temperature on contact with the sample  $\Delta T$  to the average probe temperature  $T_{\text{avg}}$ ) of a-GST/c-GST (Fig. 5(a)) and a-GT/c-GT (Fig. 5(b)) thin films are finally calculated by

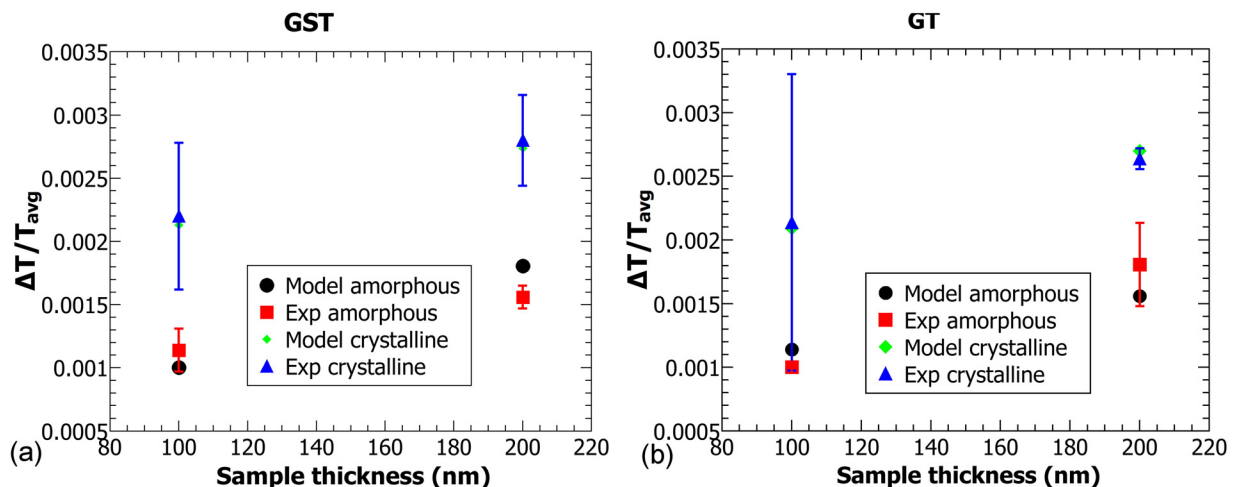


FIG. 5. Normalized thermal drop ( $\Delta T/T_{\text{avg}}$ —ratio of change of the probe temperature on contact with the sample  $\Delta T$  to the average probe temperature  $T_{\text{avg}}$ ) versus sample thickness for (a) amorphous and crystalline GST and (b) GT phases, including experimental data (with standard deviation error bars,  $N = 3$ ) and a model fit.

TABLE II. Thermal conductivities ( $\text{Wm}^{-1}\text{K}^{-1}$ ) for amorphous and crystalline phases of GST and GT, acquired by fitting the simulated temperature profile of the probe to those measured experimentally with force-displacement curves.

Phase	a-Ge <sub>2</sub> Sb <sub>2</sub> Te <sub>5</sub>	c-Ge <sub>2</sub> Sb <sub>2</sub> Te <sub>5</sub>	a-GeTe	c-GeTe
Thermal conductivity [ $\text{Wm}^{-1}\text{K}^{-1}$ ]	0.30	1.95	0.20	1.60

iteratively fitting the model to the experimentally acquired thermal drops. As presented in Table II, the resulting thermal conductivities for a-GST and c-GST are 0.30 and 1.95  $\text{Wm}^{-1}\text{K}^{-1}$ , respectively, while they are 0.20 and 1.60  $\text{Wm}^{-1}\text{K}^{-1}$  for a-GT and c-GT. These locally measured thermal conductivities for a-GST and c-GST are within the range of values determined by previous studies using more macroscopic methods, 0.19–0.33  $\text{Wm}^{-1}\text{K}^{-1}$  (Refs. 31, 44, and 45) and 1.1–2.0  $\text{Wm}^{-1}\text{K}^{-1}$ ,<sup>44,45</sup> respectively. The particularly high a-GST value may be explained by considering film preparation, where elevated temperatures during sputtering could result in the presence of a small fraction of nucleated crystalline phase as observed in separate mechanical studies<sup>46</sup> and hence a higher effective thermal conductivity. Additionally, as the experimental a-GST phase was placed between two c-GST reference lines, that may have some contribution to increased heat conduction not accounted in the model, and therefore result in a higher observed thermal conductivity. Finally, standard deviation error bars reveal a higher uncertainty for the crystalline phase of each stoichiometry. This results from a stronger variation in the experimentally measured thermal “jumps” for the crystalline regions. This can be linked to variations in the local crystallite orientations under the SThM probe and hence a wider range of directionally dependent thermal properties. The resulting a-GT and c-GT thermal conductivity values are considerably lower than those previously reported,<sup>35</sup> 2.3 and 5.7  $\text{Wm}^{-1}\text{K}^{-1}$  for a- and c-GT, respectively. However, the discrepancy in the values may be explained by the contrasting measurement methods. For example, the thermal conductivity measurements on a- and

c-GT by Nath and Chopra<sup>35,47</sup> were acquired on a 900 nm film at steady-state, by an in-plane thermal gradient over a  $4.0 \times 0.5$  cm length scale, clearly demonstrating a convergence with bulk values. Here, the thermal gradient was applied normal to the thin film surface, with heat flow considered over an area of six orders of magnitude smaller.

The TBC between GST films and substrates of different materials (C, Ti, TiN) has been calculated elsewhere using the AMM.<sup>31</sup> However, thermal time-domain thermoreflectance (TDTR) data reveal approximately one order of magnitude lower conductance values due to interfacial effects, such as grain boundaries, impurities, and surface defects.<sup>48</sup> For example, AMM values range from  $5.0 \times 10^8$  to  $3.3 \times 10^{10} \text{ W m}^{-2} \text{ K}^{-1}$  and  $5.3 \times 10^8$  to  $1.4 \times 10^{10} \text{ W m}^{-2} \text{ K}^{-1}$  for a-GST and c-GST, respectively, while TDTR values range from  $3.9 \times 10^7$  to  $5.6 \times 10^7 \text{ W m}^{-2} \text{ K}^{-1}$  for c-GST (no data are available for a-GST). The TBC values for a- and c-GST in contact with a  $\text{Si}_3\text{N}_4$  SThM probe as implemented here have not been reported, so values were calculated instead based on the acoustic mismatch and geometry,<sup>30,49</sup> specifically  $7.0 \times 10^8$  and  $3.8 \times 10^7 \text{ W m}^{-2} \text{ K}^{-1}$  (Ref. 31) between a-GST/ $\text{Si}_3\text{N}_4$  and c-GST/ $\text{Si}_3\text{N}_4$  contacts, respectively. TBC values for a-GT and c-GT in contact with the  $\text{Si}_3\text{N}_4$  probe have also not been explicitly reported, so the a-GST and c-GST values were applied; a reasonable assumption as the GST/GT Debye temperatures is similar.<sup>50,51</sup>

## CONCLUSIONS

SThM has been implemented to characterize optically switched chalcogenide phase change materials of GT and GST. Quantitative physical models together with the experimental results allowed to account for the thermal boundary conductance, and to directly determine both the thermal conductivities of the amorphous and crystalline phases as well as contact thermal resistances. The thermal conductivities for amorphous and crystalline GST are  $0.30$  and  $1.95 \text{ W m}^{-1} \text{ K}^{-1}$ , respectively. The thermal conductivities for amorphous and crystalline GT are  $0.20$  and  $1.60 \text{ W m}^{-1} \text{ K}^{-1}$ , respectively. The reported approach has been demonstrated as an effective tool for measuring thermal properties of nanoscale phase change materials, while distinguishing thermal contrast of distinct phases down to 50 nm. SThM provides an alternative characterization method to IR imaging or Raman micro-spectroscopy, and is applicable for the characterization of other thin film materials with similar low thermal conductivities.

## ACKNOWLEDGMENTS

J.B. and B.D.H. recognize DOE, Basic Energy Sciences, Electron and Scanning Probe Microscopies, Grant No. DE-SC0005037 for support. O.V.K. acknowledges support from the EPSRC Grant Nos. EP/G06556X/1, EP/K023373/1 and EU Grant Nos. QUANTIHEAT and FUNPROB. Mariia Timofeeva acknowledges the support Russian Science Foundation (Project No. 14-22-00018).

<sup>1</sup>D. Loke, T. H. Lee, W. J. Wang, L. P. Shi, R. Zhao, Y. C. Yeo, T. C. Chong, and S. R. Elliott, *Science* **336**, 1566 (2012).

- <sup>2</sup>S. R. Ovshinsky, *Phys. Rev. Lett.* **21**, 1450 (1968).  
<sup>3</sup>M. Libera and M. Chen, *J. Appl. Phys.* **73**, 2272 (1993).  
<sup>4</sup>W. Welnic, S. Botti, L. Reining, and M. Wuttig, *Phys. Rev. Lett.* **98**, 236403 (2007).  
<sup>5</sup>M. H. R. Lankhorst, B. W. S. M. M. Ketelaars, and R. A. M. Wolters, *Nature Mater.* **4**, 347 (2005).  
<sup>6</sup>M. Wuttig and N. Yamada, *Nature Mater.* **6**, 824 (2007).  
<sup>7</sup>D. Lencer, M. Salina, B. Grabowski, T. Hickel, J. Neugebauer, and M. Wuttig, *Nature Mater.* **7**, 972 (2008).  
<sup>8</sup>J. L. Bosse, I. Grishin, Y. G. Choi, B. K. Cheong, S. Lee, O. V. Kolosov, and B. D. Huey, *Appl. Phys. Lett.* **104**, 053109 (2014).  
<sup>9</sup>J. Kim, *Scanning* **32**, 320 (2010).  
<sup>10</sup>H. Bhaskaran, A. Sebastian, A. Pauza, H. Pozidis, and M. Despont, *Rev. Sci. Instrum.* **80**, 083701 (2009).  
<sup>11</sup>H. Satoh, K. Sugawara, and K. Tanaka, *J. Appl. Phys.* **99**, 024306 (2006).  
<sup>12</sup>I. Grishin, B. D. Huey, and O. V. Kolosov, *ACS Appl. Mater. Interfaces* **5**, 11441 (2013).  
<sup>13</sup>J. L. Bosse, I. Grishin, B. D. Huey, and O. V. Kolosov, *Appl. Surf. Sci.* **314**, 151 (2014).  
<sup>14</sup>W. W. Cai, A. L. Moore, Y. W. Zhu, X. S. Li, S. S. Chen, L. Shi, and R. S. Ruoff, *Nano Lett.* **10**, 1645 (2010).  
<sup>15</sup>A. A. Balandin, S. Ghosh, W. Z. Bao, I. Calizo, D. Teweldebrhan, F. Miao, and C. N. Lau, *Nano Lett.* **8**, 902 (2008).  
<sup>16</sup>A. Majumdar, *Annu. Rev. Mater. Sci.* **29**, 505 (1999).  
<sup>17</sup>M. A. Lantz, B. Gotsmann, U. T. Durig, P. Vettiger, Y. Nakayama, T. Shimizu, and H. Tokumoto, *Appl. Phys. Lett.* **83**, 1266 (2003).  
<sup>18</sup>M. E. Pumarol, M. C. Rosamond, P. Tovee, M. C. Petty, D. A. Zeze, V. Falko, and O. V. Kolosov, *Nano Lett.* **12**(6), 2906 (2012).  
<sup>19</sup>J. H. Coombs, A. P. J. M. Jongenelis, W. Vanesspiekman, and B. A. J. Jacobs, *J. Appl. Phys.* **78**, 4918 (1995).  
<sup>20</sup>F. Yang, L. Xu, R. Zhang, L. Geng, L. Tong, J. Xu, W. N. Su, Y. Yu, Z. Y. Ma, and K. J. Chen, *Appl. Surf. Sci.* **258**, 9751 (2012).  
<sup>21</sup>S. Kumar, D. Singh, S. Sandhu, and R. Thangaraj, *Phys. Status Solidi A* **209**, 2014 (2012).  
<sup>22</sup>M. Chirtoc, X. Filip, J. F. Henry, J. S. Antoniow, I. Chirtoc, D. Dietzel, R. Meckenstock, and J. Pelzl, *Superlattices Microstruct.* **35**, 305 (2004).  
<sup>23</sup>P. Gossel, O. Raphael, F. Depasse, T. Duvaut, and N. Trannoy, *Int. J. Therm. Sci.* **46**, 980 (2007).  
<sup>24</sup>P. Tovee, M. E. Pumarol, D. A. Zeze, K. Kjoller, and O. Kolosov, *J. Appl. Phys.* **112**, 114317 (2012).  
<sup>25</sup>K. Feldman, T. Tervoort, P. Smith, and N. D. Spencer, *Langmuir* **14**, 372 (1998).  
<sup>26</sup>L. Shi and A. Majumdar, *Trans. ASME J. Heat Transfer* **124**, 329 (2002).  
<sup>27</sup>See supplementary material at <http://dx.doi.org/10.1063/1.4895493> for detailed procedure of SThM calibration.  
<sup>28</sup>P. D. Tovee, M. E. Pumarol, M. C. Rosamond, R. Jones, M. C. Petty, D. A. Zeze, and O. V. Kolosov, *Phys. Chem. Chem. Phys.* **16**, 1174 (2014).  
<sup>29</sup>P. D. Tovee and O. V. Kolosov, *Nanotechnology* **24**, 465706 (2013).  
<sup>30</sup>J.-L. Battaglia, V. Schick, C. M. Rossignol, A. Kusiak, I. Aubert, A. Lamperti, and C. Wiemer, *Appl. Phys. Lett.* **102**, 181907 (2013).  
<sup>31</sup>E. Bozorg-Grayeli, J. P. Reifenberg, K. W. Chang, M. Panzer, and K. E. Goodson, "Thermal conductivity and boundary resistance measurements of GeSbTe and electrode materials using nanosecond thermoreflectance" in *2010 12th IEEE Intersociety Conference on Thermal and Thermomechanical Phenomena in Electronic Systems* (IEEE, 2010).  
<sup>32</sup>J. Reifenberg, E. Pop, A. Gibby, S. Wong, and K. Goodson, in *Proceedings of the 10th Intersociety Conference on Thermal and Thermomechanical Phenomena in Electronics Systems, IOTHERM 2006*, 30 May–2 June 2006, Vol. 106.  
<sup>33</sup>L. J. Challis, *J. Phys. C* **7**, 481 (1974).  
<sup>34</sup>H. S. P. Wong, S. Raoux, S. Kim, J. L. Liang, J. P. Reifenberg, B. Rajendran, M. Ashghii, and K. E. Goodson, *Proc. IEEE* **98**, 2201 (2010).  
<sup>35</sup>P. Nath and K. L. Chopra, *Phys. Rev. B* **10**, 3412 (1974).  
<sup>36</sup>G. C. Sosso, D. Donadio, S. Caravati, J. Behler, and M. Bernasconi, *Phys. Rev. B* **86**, 104301 (2012).  
<sup>37</sup>J. Lee, Z. J. Li, J. P. Reifenberg, S. Lee, R. Sinclair, M. Ashghii, and K. E. Goodson, *J. Appl. Phys.* **109**, 084902 (2011).  
<sup>38</sup>T. J. Zhu, H. L. Gao, Y. Chen, and X. B. Zhao, *J. Mater. Chem. A* **2**, 3251 (2014).  
<sup>39</sup>J. H. Lienhard, *A Heat Transfer Textbook* (Phlogiston Press, Cambridge, MA, 2008).  
<sup>40</sup>C. Y. Ho, R. W. Powell, and P. E. Liley, *J. Phys. Chem. Ref. Data* **1**, 279 (1972).

- <sup>41</sup>L. P. B. M. Janssen and C. G. Warmoeskerken, *Transport Phenomena Data Companion* (Edward Arnold, 1987).
- <sup>42</sup>W. M. Haynes, *CRC Handbook of Chemistry and Physics* (CRC Press, 2012).
- <sup>43</sup>V. Weidenhof, I. Friedrich, S. Ziegler, and M. Wuttig, *J. Appl. Phys.* **86**, 5879 (1999).
- <sup>44</sup>H. K. Lyeo, D. G. Cahill, B. S. Lee, J. R. Abelson, M. H. Kwon, K. B. Kim, S. G. Bishop, and B. K. Cheong, *Appl. Phys. Lett.* **89**, 151904 (2006).
- <sup>45</sup>J. L. Battaglia, A. Kusiak, V. Schick, A. Cappella, C. Wiemer, M. Longo, and E. Varesi, *J. Appl. Phys.* **107**, 044314 (2010).
- <sup>46</sup>J. L. Bosse, P. D. Tovee, B. D. Huey, and O. V. Kolosov, *J. Appl. Phys.* **115**, 144304 (2014).
- <sup>47</sup>P. Nath and K. L. Chopra, *Thin Solid Films* **18**, 29 (1973).
- <sup>48</sup>J. P. Reifenberg, K. W. Chang, M. A. Panzer, S. Kim, J. A. Rowlette, M. Asheghi, H. S. P. Wong, and K. E. Goodson, *IEEE Electron Device Lett.* **31**, 56 (2010).
- <sup>49</sup>K. Børkje and S. Girvin, *New J. Phys.* **14**, 085016 (2012).
- <sup>50</sup>H. Wang, Y. Xu, M. Shirnono, Y. Tanaka, and M. Yarnazaki, *Mater. Trans.* **48**, 2349 (2007).
- <sup>51</sup>Y. Ishihara, Y. Yoshita, and I. Nakada, *J. Phys. Soc. Jpn.* **55**, 1948 (1986).